

Title: Measuring theoretical descriptors of the oxygen evolution reaction: Free energy difference to create Ti-OH* by time-resolved optical spectroscopy

Authors: Ilya Vinogradov^α, Suryansh Singh^{α,γ}, Hanna Lyle^{α,γ}, Michael Paolino^{α,λ}, Aritra Mandal^{α,*}, Jan Rossmeisl^χ, and Tanja Cuk^{α,⊥*}

Affiliations:

^αRenewable and Sustainable Energy Institute (RASEI), University of Colorado, Boulder, Boulder, 80303

^γMaterials Science and Engineering Program, University of Colorado, Boulder, Boulder, 80303

^λDepartment of Physics, University of Colorado, Boulder, Boulder, 80303

^χDepartment of Chemistry, University of Copenhagen, Copenhagen, Denmark

[⊥]Department of Chemistry, University of Colorado, Boulder, Boulder, 80303

*Corresponding Authors: tanja.cuk@colorado.edu, aritra.mandal@colorado.edu

Abstract:

Theoretical descriptors differentiate the catalytic activity of materials for the oxygen evolution reaction (OER) by the strength of oxygen binding in the reactive intermediate created upon electron transfer. Recently time-resolved spectroscopy of (*photo*)-electrochemically driven OER followed the vibrational and optical spectra of this intermediate, denoted M-OH*. However, these inherently kinetic experiments have not been connected to the relevant thermodynamic quantities. Here, we discover that picosecond optical spectra of the Ti-OH* population on lightly doped SrTiO₃ are modulated by a shift in the surface hydroxylation. A Langmuir isotherm as a function of pH extracts an effective equilibrium constant (K_{eff}) relatable to the free energy difference of the first OER reaction step ($\Delta G_1(\text{OH}^*)$). That free energy differences of the catalytic surface are definable through a time-resolved spectroscopy provides a new and critical connection between theory and experiment by which to tailor the pathway of water oxidation and other surface reactions.

Introduction:

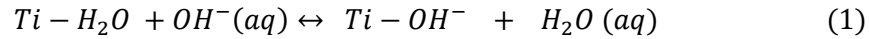
Catalytic reactions are described by a set of meta-stable intermediate chemical forms that reorganize reactants into products¹. Yet, the activity of material surfaces for catalysis has been differentiated largely by their cumulative product evolution, with a primary example being the steady-state current in electrochemical measurements². Given several underlying and separate reaction steps, multiple mechanistic models could explain the same outcome³⁻⁵. Thus, there exists a need for experiments to access the individual reaction steps⁴⁻⁵. To do so through the free energy differences (ΔG) between intermediates would directly underpin the theory⁶ and would provide thermodynamic quantities by which to tailor the material and its environment for desired functionality⁷.

One of the most important and studied reactions in this context is the electrochemically-driven oxygen evolution reaction (OER) from water on transition metal oxide surfaces⁸⁻⁹. The M-OH*

intermediate, created upon the first electron and proton transfer, is expected to initiate the formation of the first chemical bond of O₂ (O-O), with corresponding $\Delta G_1(\text{OH}^*)$ and $\Delta G_3(\text{O-O})$ ^{6, 10}. With scaling relationships¹¹, $\Delta G_1(\text{OH}^*)$ becomes a predictive theoretical descriptor: when $\Delta G_1(\text{OH}^*)$ is large, forming M-OH* is rate-limiting and when it is small, forming the O-O bond is rate-limiting. However, to date, while electrochemical current defines the “y-axis” of catalytic activity, the $\Delta G_1(\text{OH}^*)$ descriptor on the “x-axis” is largely computational.

A series of time-resolved studies of photo-electrochemically driven OER have isolated the spectral and kinetic signatures of M-OH*, including titanium oxyls (Ti-O⁻ terminal and Ti-O⁺-Ti in-plane)¹²⁻¹³, the cobalt oxo (Co=O)¹⁴, and the iron oxo (Fe=O)¹⁵. The M-OH* notation is generic for all these species, with H⁺ either bound to the oxygen site or having transferred to a nearby one¹⁶⁻¹⁷. While vibrational spectroscopies determine these detailed bonding geometries¹⁸⁻¹⁹, optical spectroscopy^{12, 20} revealed easily-trackable electronic levels created in the middle of the semiconducting band gap that target the total population of M-OH*. Ultrafast studies of SrTiO₃ (STO) followed the picosecond formation of the Ti-OH* population from delocalized semiconductor holes¹² and its subsequent, microsecond decay towards the next reaction step²¹.

While such time-resolved studies structurally identified transient surface intermediates and provided insight into their role in the catalytic cycle, comparatively little experimental information exists on their energetics. The difficulty lies in finding a methodology that both isolates the reaction steps and captures their thermodynamic properties²²⁻²³. In photo-electrochemistry, light excites the reaction instantaneously from the surface defined by the dark equilibrium with the electrolyte. Therefore, the proton and electron transfer of the first OER step can be well separated, with the proton transfer occurring in the dark and the electron transfer occurring only upon creation of VB holes:



Together, these constitute $\text{Ti} - \text{OH}_2 \rightarrow \text{Ti} - \text{OH}^* + \text{H}^+ + e^-$, the first step in the OER mechanism; the * notation here refers to the hydroxylated site upon electron transfer. While the first reaction is an explicit equilibrium, the second forms a meta-stable species, with free-energy differences ΔG_{OH^-} (of the surface acidity or pK_a) and $\Delta G_{\text{OH}^*}(\text{U}_{\text{VB}})$ (of VB hole-trapping). By being separable, the surface hydroxylation prior to light excitation can shift the reaction equilibria, which allows this work to identify $\Delta G_1(\text{OH}^*)$ by time-resolved optical spectra. In particular, the sigmoidal pH dependence of the picosecond Ti-OH* population generates a Langmuir isotherm of a meta-stable intermediate on the driven surface. For surfaces in which the hydroxylation can be modulated in an accessible pH range, the work closes a vital missing gap between

theoretical descriptors of surface catalysis and experiments that identify the structure and reaction kinetics of intermediates.

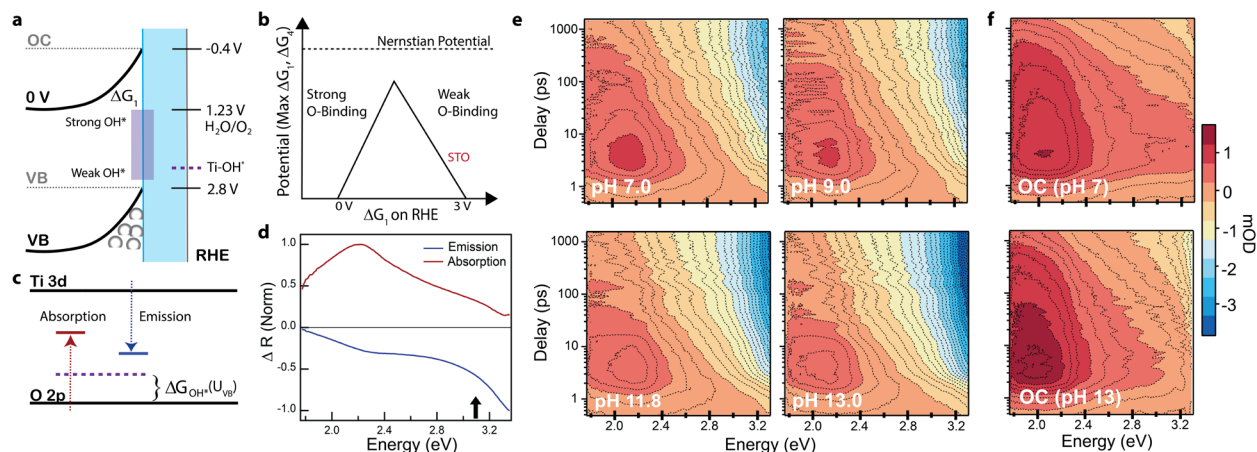


Figure 1: Photo-electrochemical configuration and optical spectra. a) Cartoon of energy level alignments at closed (0 V vs. SCE) and at open circuit (OC) on the RHE scale (pH 0). b) Volcano plot of OER theoretical analysis, depicting strong and weak oxygen-binding branches c) Cartoon of the optical transitions induced by Ti-OH* intermediates, leading to emission (blue arrow) and absorption (red arrow). The dashed purple level corresponds to the redox level for creating Ti-OH*, also depicted in a). The optical transitions are vertical ones, which involve states in the CB and VB respectively that are at the reaction coordinate of the distorted Ti-O bonds in Ti-OH*; the difference in the blue and red lines reflects that these are unique for the CB and VB. d) Emission and absorption derived by a constrained, singular value decomposition of the optical spectra in e) Transient optical spectra of the absorption (red) and emission (blue) in the visible regime for select pH at closed circuit. From the raw data, the acoustic phonon oscillations have been removed. f) Transient optical spectra at open circuit for pH 7 and pH 13 on the same mOD scale as the closed circuit data.

Transient Optical Spectra of the Electrochemical Interface

Figure 1 shows the primary pH-dependent optical spectra from which we draw our conclusions. The transient data are taken under steady-state conditions of photo-electrochemical O₂ evolution using pulsed (150 fs, 500 Hz) band-gap (266 nm, 4.66 eV) excitation of n-SrTiO₃ (0.1%, 0.5%, and 0.7% Nb STO) described previously and in detail in Fig. S1-S3. Here, the surface is probed by a broad-band optical pulse (375-700 nm, 1.7-3.3 eV). While the current is approximately Faradaic for O₂ evolution alongside a high-quantum efficiency of charge separation (~75%), side-reactions do affect the sample surface²⁴. Therefore, to obtain the high-quality kinetic data, we employ a continuous scanning method (Fig. S4). At a photo-excitation density of 0.04 mJ/cm², one maintains a constant steady-state current to within 0.5% in a single measurement (Fig. S3) and which corresponds to a turn-over frequency ~1 O₂/site-sec of the illuminated area. The cartoon (Fig. 1a) shows the level alignment of the valence and conduction bands of SrTiO₃ with the Nernstian potential of water oxidation on the RHE scale. The primary data are taken with a constant 0 V vs. SCE applied to the back of the electrode. A constant 0 V vs. SCE is chosen to maintain the same potential drop across the part of the electric double layer that involves free ions in the electrolyte (phosphate, sulfate, OH⁻, H⁺), such that reaction (1) can be considered fairly independently of salt concentration (Fig. S2). With this electrochemical configuration, the Schottky barrier will necessarily increase with pH due to the interfacial Ti-OH⁻ dipole²⁵ (Fig. S1-S2). Data taken at open circuit (OC) aids in the assignment of spectral components and in the interpretation of the pH dependence. Finally, 0.1% Nb

and 0.7% Nb STO were characterized for hydroxylation at near neutral conditions by Ambient Pressure X-ray Photoelectron Spectroscopy (AP-XPS) (Fig. S5).

Upon excitation, a delocalized hole in the valence band can relax to create Ti-OH^* . When a hole traps to an oxygen site, the Ti-O distances distort and mid-gap levels form, as described in detail for TiO_2 ¹⁶⁻¹⁷ and for SrTiO_3 ^{12,26-27}. As shown schematically in Fig. 1a (purple dotted line), these mid-gap levels are relatable to the redox level of $\Delta G_1(\text{OH}^*)$ by $\Delta G_{\text{OH}^*}(U_{\text{VB}})$ of reaction (2):

$$\Delta G_1(\text{OH}^*) = \text{VB (RHE)} + \Delta G_{\text{OH}^*}(U_{\text{VB}})(\text{eV}) \quad (3)$$

Here, the pH dependence of reaction (1) is that of the RHE scale (-59 mV/pH), which is physically associated with the interfacial dipole of the VB edge.²⁵ With eq. (3), the $\Delta G_1(\text{OH}^*)$ for different materials can be placed within the band-gap of STO (Fig. 1a), rising within the gap and lower on the RHE scale for stronger oxygen binding within M-OH^* (Fig. 1b).

Emissive optical transitions in the visible regime (blue arrow, Fig. 1c) result from CB electrons to the newly created Ti-OH^* at the distorted reaction coordinate (blue line, Fig. 1c). Photoluminescence of STO samples routinely assigns the spontaneous emission peaked between 2.4 - 2.8 eV to localized holes^{26,28-29}. The recent transient optical spectroscopy during OER characterized the stimulated emissive optical dipole transitions¹² by a 1.3 ps kinetic growth which also occurred in the vibrational spectroscopy identifying the titanium oxyl (Ti-O^\cdot). Here, the broad-band probe records this emission in time for lightly doped Nb 0.1% STO (Fig. 1e). From these optical spectra, acoustic phonon oscillations have been subtracted out (Fig. S6). The emission (blue) appears clearly during *in-situ* OER and increases with higher pH (Fig. S7) but is independent of salt concentration (Fig. S8); at OC conditions for which electrons can more easily recombine with Ti-OH^* , the emission is much less pronounced but has the same trend with pH and salt (Fig. S7-S8). Moreover, the emission appears dominantly as a ~2 ps kinetic growth after the initial excitation, as expected for an exoergic $\Delta G_{\text{OH}^*}(U_{\text{VB}})$, with the time constant assigned previously¹².

Alongside this emissive transition, an absorptive transition (red arrow, Fig. 1c) also exists. We find the absorption to be less sensitive to the Ti-OH^* population: the absorption appears most prominently at open circuit, exhibits decay kinetics, and is not significantly modulated by surface conditions (pH). An absorptive transition in the visible regime could arise from VB electrons promoted to an excited potential energy surface (red line, Fig. 1c) for which the Ti-O distortion of Ti-OH^* is maintained while leaving behind a VB hole, as proposed for titania¹⁶ and other transition metal oxides³⁰⁻³¹. A red-shifted absorption to the emission has been attributed to, in iron oxide²⁰, the intermediate population but in a variety of oxides, the valence band hole population³²⁻³⁴. Since the proposed absorptive transition is modulated by the VB density of states for hole occupation, a function of both trapped and VB holes, one might expect the kinetics to exhibit a complex interplay of the two populations. In contrast, the CB electron density of states responsible for the emissive transition is independent of the trapped hole population. The anticipated optical transitions are further discussed in Fig. S9.

Principal Component Analysis of the Optical Spectra:

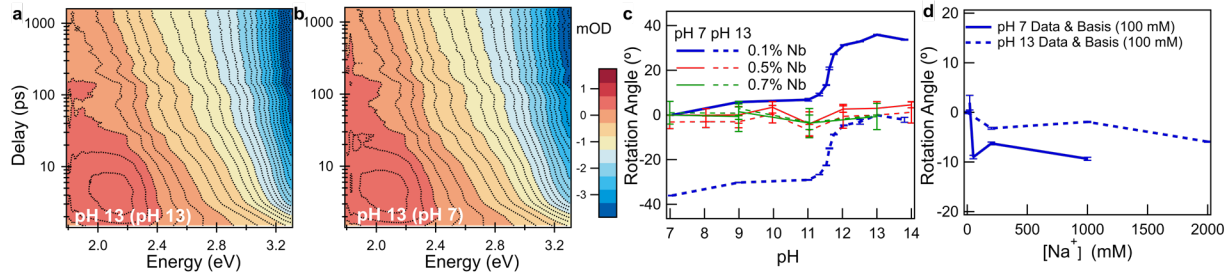


Figure 2: Singular value decomposition (SVD) and rotation analysis for the closed circuit data. a) Reconstruction of the pH 13 spectrum from its first two SVD components. b) Reconstruction of the spectrum in a) from the spectral SVD components of the pH 7 transient optical spectra c) Rotation angle analysis for the phosphate buffered pH data set showing a sigmoidal trend across pH in 0.1% Nb STO. The angle is given relative to the pH 7 data in solid lines and relative to the pH 13 data set in dotted lines. Data are shown for all three STO samples (0.1%, 0.5%, and 0.7% Nb). d) Rotation angle analysis for the data set showing little trend with salt concentration for pH 7 (red) and pH 13 (blue) in a Na₂SO₄/NaOH solution. In both pH 7 and pH 13, the reference spectral components are from the corresponding 100 mM [Na⁺] spectral map. For c) and d), error bars indicate the standard deviation of the four angles in the rotation matrix R , which measures how orthogonal the transformation is between the reference and final spectral components.

The spectra shown in Fig. 1d are the result of a principal component analysis constrained³⁵⁻³⁶ to have a pure emissive component and an absorptive one. We first show how two predominant spectral components exist in common for the full data set. Singular Value Decomposition³⁷ (SVD, Fig. S10) directly yields two dominant components for each reaction condition. If these are common to the data set, one should be able to reconstruct one reaction condition's optical spectra from a linear combination of the principle components of another, or

$$M^{(pH\ 13)} \approx \left(U_{1,2}^{(pH\ 7)} \cdot R^{-1} \right) \cdot S_{1,2}^{(pH\ 13)} \left(V_{1,2}^{(pH\ 13)} \right)^T, \quad (4)$$

The columns of $U_{1,2}^{(pH)}$ and $V_{1,2}^{(pH)}$ are orthonormal and represent the SVD spectra and kinetics, respectively. The linear combination matrix is $R = \left(U_{1,2}^{(pH\ 13)} \right)^T U_{1,2}^{(pH\ 7)}$. If a common two component basis exists, R will be a rotation matrix (accounting for reflections).

We show the similarity between the pH 13 data set reconstructed from its own two SVD components in Fig. 2a and the pH 7 SVD components in Fig. 2b. The rotation matrix can be calculated for any pair of reaction conditions within a data set with small error bars. This rotation analysis shows a sigmoidal pH dependence already encoded in the 0.1% Nb STO data without constraints (Fig. 2c) and quantifies little dependence of the spectral components on the salt concentration (Fig. 2d). It also shows little pH dependence for highly doped (0.5%, 0.7% Nb) STO (Fig. 2c).

Shifting the Reaction Equilibria of the Ti-OH^* Population by pH:

While the above establishes a clear and quantifiable trend in pH exists, it does not in itself assign a spectral component to the Ti-OH^* population and its origin from reaction (2). We start with a cartoon of the hydrated STO surface in the dark and under photo-excitation (Fig. 3a). The un-doped STO surface is understood to partially dissociate H_2O at neutral conditions³⁸⁻⁴⁰, such that approximately half the titania sites are water absorbed and half hydroxylated. The lightly doped 0.1% Nb STO surface exhibits a similar ratio of hydroxylation to water absorption by AP-XPS in Fig. S5. Since they are separated by Ti-OH_2 groups, the isolated Ti-OH^- are well-positioned to trap holes quickly (reaction 2). Further, given the above dichotomy between the emission and absorption, a constrained SVD analysis identifies the fast rise-component of the Ti-OH^* population using:

$$M \approx (U_{1,2} \cdot X) \cdot (X^{-1}S_{1,2}(V_{1,2})^T), \quad (5)$$

X is a new matrix which describes the projection of the raw SVD components $U_{1,2}$ onto purely emissive (1) and absorptive (2) spectral components. The procedure is outlined in the supplemental information (Section VI, Fig. S11). The emissive spectrum (Fig. 1c) increases beyond the band gap energy, as expected for probe-stimulated electrons stimulated with an increasing density of states away from the CB edge. The absorptive spectrum has a peak near ~ 2 eV as identified in a number of other oxides^{16, 30-31}.

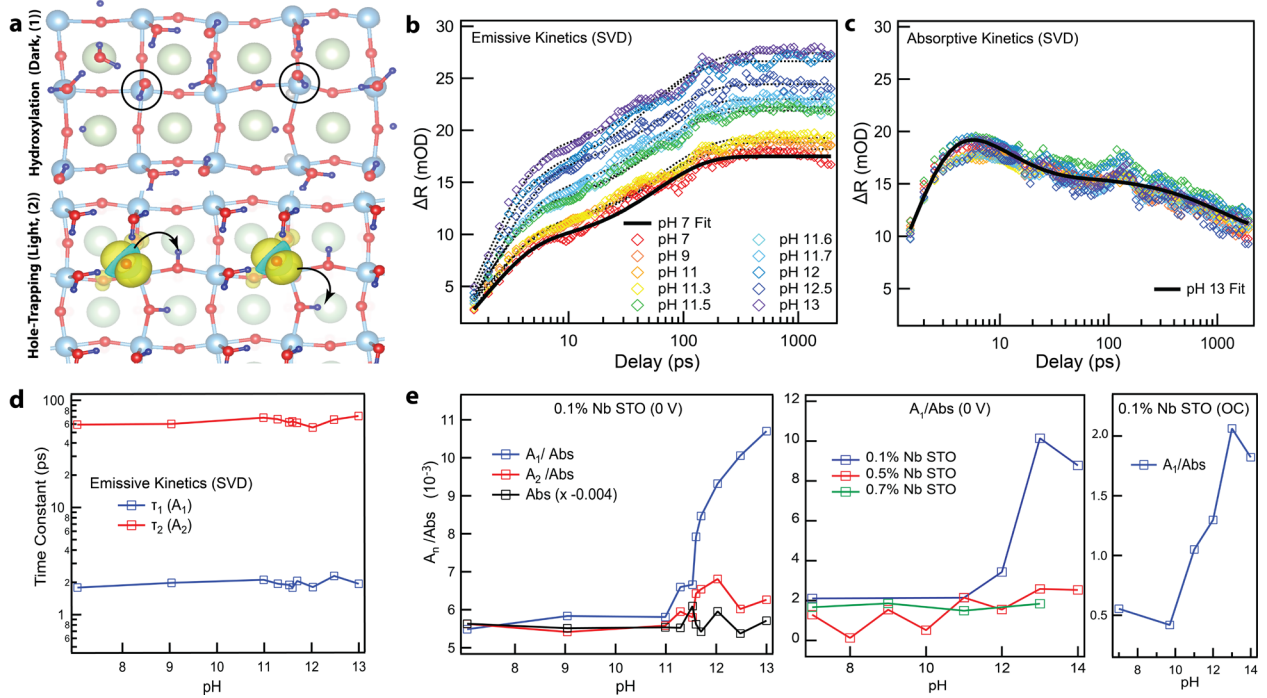


Figure 3: Constrained SVD analysis for 0.1% Nb STO phosphate-buffered data at closed circuit unless otherwise specified. a) Cartoon of the 0.1% Nb STO surface in the dark and upon light excitation, reflecting the two separable proton and electron transfer steps. b) Weighted, emissive growth kinetics $(X^{-1}S_{1,2}(V_{1,2})^T)_1$ as a function of pH (colored diamonds) fit with two rising exponentials (black solid and dotted lines). c) The same as a), but for the weighted, absorptive decay kinetics $(X^{-1}S_{1,2}(V_{1,2})^T)_2$. d) The time constants of the two rising exponentials for the emissive kinetics as a function of pH. e) The populations (A_1, A_2) defined by the two time constants, normalized by the integrated absorption (A_n/Abs), as a function of pH; the integrated absorptive signal (Abs), as a function of pH. Alongside, A_1/Abs is compared for the three n-STO samples, 0.1%, 0.5%, and 0.7% Nb, taken on the same optical setup. A_1/Abs is shown for 0.1% Nb STO under OC conditions with sulfate buffer.

Fig. 3b shows the constrained kinetics associated with emission, $(X^{-1}S_{1,2}(V_{1,2})^T)_1$, for each pH at 0 V vs. SCE. While the kinetics exhibit consistent growth rates across pH, the response amplitude systematically increases with pH. On the other hand, the kinetics associated with absorption, $(X^{-1}S_{1,2}(V_{1,2})^T)_2$, exhibits decay kinetics and shows little change with pH (Fig. 3c). Fitting the emissive curve with two rising exponentials defines the two time scales ($\tau_1 \sim 2$ ps and $\tau_2 \sim 60$ ps) shown in Fig. 3d. Since the time-integrated absorption is independent of pH, we can use it to normalize the emission for fluctuations in pump-probe overlap. In Fig. 3e, we show the normalized emissive response as a function of pH and for different experimental conditions. For 0.1% Nb STO, the amplitude of the fast, 2 ps rise (A_1) has a clear sigmoidal dependence on pH centered at 11.7. On the other hand, the same analysis of 0.5% and 0.7% Nb STO shows little pH dependence, reflecting the rotation analysis (Fig. 2c); the highly doped STO optical data is shown (Fig. S12) and analyzed further (Fig. S13-S14) in Section VII of the supplemental. For 0.1% Nb STO, the amplitude of the 60 ps rise (A_2) is also fairly pH-independent. While in this analysis A_1 and A_2 both report on the Ti-OH^* population, since A_2 occurs later, A_2 either represents a time-evolution of the 2 ps Ti-OH^* population or a separate population of Ti-OH^* arising from a different source. While the pH dependence shown in Fig. 1 and Fig. 3 is taken with a phosphate buffered solution that allows for finer steps in pH, a sigmoidal pH dependence also occurs for A_1 with a sulfate solution (Fig. S15). Importantly, the same methodology extracts a sigmoidal pH dependence from the OC data (Fig. 3e and Fig. S16) for which no surface degradation exists and photo-excitation flattens the Schottky barrier; this helps isolate the effect as coming from the interfacial hydroxylation.

These results establish a sigmoidal pH dependence for the 2 ps component of Ti-OH^* creation from VB holes, which reflects a reaction isotherm and the two reaction steps proposed above. The fast time-scale for the A_1 population aids in separating reaction (1) from (2), since any re-equilibration with OH^- in solution should occur at significantly longer time-scales⁴¹⁻⁴². It also suggests that the hole-transfer occurs without a simultaneous full proton transfer to solution as anticipated by AIMD simulations on titania¹⁶⁻¹⁷. The absence of a clear H/D kinetic isotope effect (Fig. S17) substantiates the lack of a free H^+ as a product⁴³⁻⁴⁴.

The two separable reactions are also supported by investigating a similar sample, but for which the surface is expected to be hydroxylated already under neutral conditions. 0.7% Nb STO indeed exhibits a much higher hydroxylation than 0.1% Nb STO by AP-XPS, with a factor of 2-3 increase (Fig. S5); the more electron dense, in-plane, lattice oxygen sites can promote H_2O dissociation. Since the optical spectra for both 0.5% and 0.7% Nb STO also do not exhibit a resolvable pH-dependence, the results reflect a dark equilibrium which cannot be pushed by pH in basic conditions. The picture of a two-dimensional network for hole-delocalization within the hydroxylated surface emerges in highly doped STO, in contrast to the more isolated Ti-OH^- sites in lightly doped STO.

Langmuir Isotherm Model & Quasi-equilibrium Constant for Ti-OH^* Population:

The free energies of the relevant steps are depicted within the full photo-driven OER reaction in Fig. 4a. ΔG_{OH^-} is described by the chemical potential of Ti-OH^- relative to Ti-OH_2 along the same, free energy surface in the dark (solid black lines). On the other hand, reaction (2) involves a crossing of two distinct surfaces, where the light pulse (yellow arrow) first creates the hole on the oxidized surface at the

reaction coordinate defined by the reduced VB but then quickly transfers to the surface for which the trapped hole, Ti-OH^* , is a minimum.

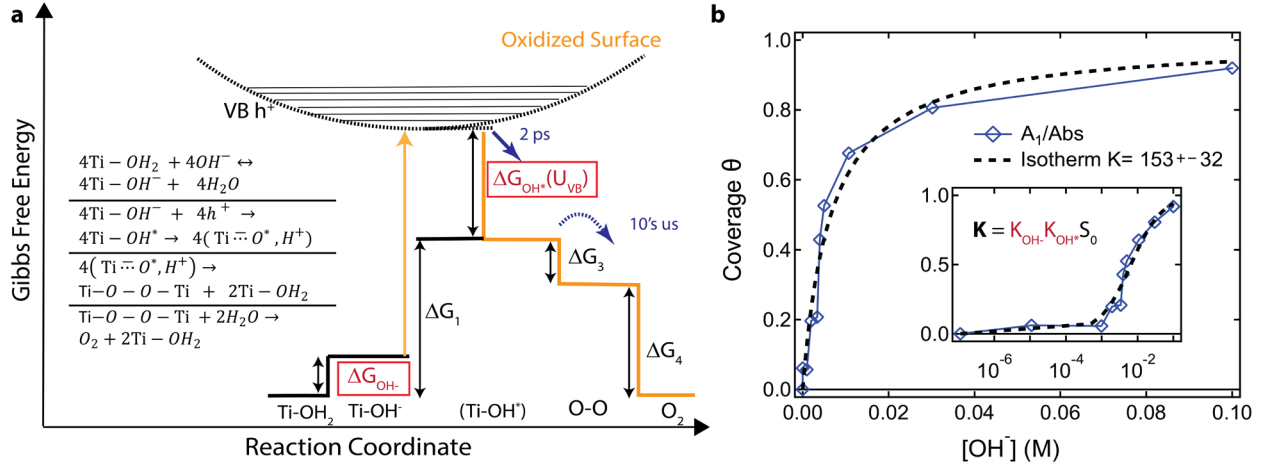


Figure 4: (a) Free energy diagram of Ti-OH^- adsorption and Ti-OH^* creation in the context of the full reaction scheme. Photo-excitation (yellow arrow) separates the diagram into the equilibrated and driven surfaces. The black dotted line represents the excited hole in the VB, while the yellow solid line represents the pathway to O_2 for a photo-excited hole. The ΔG for each reaction step per site in OER is shown in the standard state, with the ones relevant to the experiment highlighted in red. The time constant (2 ps) for Ti-OH^* creation from the VB hole highlighted in this work is shown by the blue arrow; the dotted blue arrow (10's μs) denotes the downhill reaction kinetics for O-O bond formation, as suggested by previous work²¹. The full, multi-site reaction scheme suggested by this diagram is stated to the left. (b) The A_1/Abs component (blue triangles) of 0.1% Nb STO in Figure 3e, where the pH 7 contribution has been subtracted and the pH 14 contribution is normalized to 1. The data points have been fit to the Langmuir isotherm described by eq. 6 & 7 in the text, with coverage $\theta = \frac{[\text{Ti-OH}^*]}{[h_0^+]}$ and $K_{\text{eff}} = 153 \pm 32$. The inset shows the agreement on a logarithmic scale with the characteristic sigmoidal behavior of an isotherm.

We now turn to the description of the reaction isotherm using a phenomenological model. The model and its application, summarized in this section, is developed in detail in Section X of the Supplementary Information. If a limiting surface site density (S_0) is involved, occupied (S-A) and unoccupied (S) sites are restricted to exchange with each other ($S_0 = S + \text{S-A}$) and a Langmuir-type isotherm is anticipated⁴⁵. For reaction (1), this surface limitation is simply the total surface Ti-site density, S_0 , such that $S_0 = [\text{Ti-OH}^-] + [\text{Ti-OH}_2]$. On the other hand, reaction (2) involves an exchange between delocalized and trapped holes. The surface limitation is therefore $h_0^+ = [h^+] + [\text{Ti-OH}^*]$, where h_0^+ represents the total hole density excited by the laser in a single pulse, a constant and equal to at most 2% of the surface site density. The $[\text{Ti-OH}^-]$ coverage can then fairly independently modulate the isotherm for $[\text{Ti-OH}^*]$ coverage, as suggested by the sigmoidal dependence in the data itself. Since the experimental variable is the bulk $[\text{OH}^-]$ in solution, the two reaction isotherms should be combined using the $[\text{Ti-OH}^-]$ coverage. The resulting equation and its effective equilibrium constant are:

$$\theta = \frac{[\text{Ti-OH}^*]}{[h_0^+]} = \frac{K_{\text{eff}}[\text{OH}^-]}{1 + K_{\text{eff}}[\text{OH}^-]} \quad (6)$$

$$K_{\text{eff}} = K_{\text{OH}^-} K_{\text{OH}^*} S_0 \quad (7)$$

In the above, $K_{\text{OH}^-} = [\text{Ti-OH}^-]/[\text{Ti-OH}_2][\text{OH}^-]$, $K_{\text{OH}^*} = [\text{Ti-OH}^*]/[\text{Ti-OH}^-][h^+]$, and S_0 is the surface site density, such that K_{eff} carries a total unit of M^{-1} . The sigmoidal dependence of the extracted coverage is

well described by an isotherm with a fitting constant of $K_{eff} = 153$ reflecting the pH=11.7 half-rise. It is important to note that this K_{eff} is in the context of a continually downhill catalytic cycle for which a meta-stable population is being isolated, rather than a reaction that reaches completion.

We now estimate the anticipated value of K_{eff} from theoretical calculations. Theoretically, each VB hole is tied to a Ti-OH⁻ surface site and doesn't appear as a separate concentration⁴⁶. Therefore, obtaining a theoretical equilibrium constant, K_{eff}^{calc} , requires dividing K_{eff} by $[h_0^+]$, which represents the degeneracy of the VB hole states upon photo-excitation. With a pK_a of the Ti-OH₂ site of 8⁴⁷ and a $\Delta G_{OH^*}(U_{VB}) = -0.4$ eV^{12, 26}, the derived measured value ($K_{eff} \sim 5$ with a half-rise near pH 13) comes within a factor of ~20 of the observed $K_{eff} \sim 150$. However, this is approximate since calculated $\Delta G_{OH^*}(U_{VB})$ vary and not all holes need to arrive as Ti-OH* through hydroxylated sites modulated by pH in basic conditions. We leave this quantification for future work.

We now obtain the electrochemically driven redox level for the first proton and electron transfer of the OER scheme. Using eq. 3, with a calculated $\Delta G_{OH^*}(U_{VB}) = -0.4$ eV consistent with the isotherm and a 2.8 V VB vs. RHE for STO²⁵, $\Delta G_1(OH^*) = 2.4$ V vs. RHE in the standard state, which places STO comfortably on the weak-binding branch of the volcano¹⁰⁻¹¹. In applying eq. (3), $\Delta G_{OH^*}(U_{VB})$ is considered constant for a particular surface across the pH range. Further insight into the weak binding derives from how much $\Delta G_{OH^*}(U_{VB})$ leads to a sigmoidal half-rise close to the pK_a of Ti-OH₂: it occurs at pH 11.7 rather than at 8⁴⁷. An increasingly more exoergic $\Delta G_{OH^*}(U_{VB})$ on the RHE scale would be needed to obtain a half-rise closer to 8. The weak-binding and the downhill pathway towards O-O bond formation observed previously²¹ supports the full multi-site reaction mechanism of Fig. 4a, where the first electron-transfer creates four Ti-OH* intermediates from four H₂O and then subsequent thermo-chemical reaction steps form O₂ and release two H₂O.

Conclusions:

This work discovers a methodology for obtaining equilibrium constants of meta-stable surface intermediates of a driven catalytic reaction using Langmuir isotherms and time-resolved optical spectra of the intermediate population. In particular, we constructed an effective equilibrium constant that defines the reactive Ti-OH* population during water oxidation to O₂. It is in the range of 10² due primarily to the combination of an endoergic ΔG_{OH^-} for surface hydroxylation and an exoergic $\Delta G_{OH^*}(U_{VB})$ for photo-excited VB holes. The results shown here make recent time-resolved spectroscopic investigations of the water oxidation reaction germane by uniquely establishing a necessary connection to theoretical free energy differences. In this regard, the work finds experimental evidence to define where SrTiO₃ occurs on the x-axis of water oxidation volcano plots, which underpins titania as an electro-catalyst whose energy efficiency is limited by creating rather than removing bound Ti-OH* intermediates.

Methods:

Working Electrode & Spectro-electrochemical Measurements. 0.08% Nb-doped SrTiO₃ by weight (henceforth 0.08% is referred to as 0.1%) SrTiO₃ single crystals of size 10x10x0.5 mm with crystallographic orientation (100) and polished front sides ($R_a < 5$ Å) and unpolished backsides were obtained from MTI Corp. (Richmond, CA). All spectroscopic measurements were performed on the polished front sides. Spectro-electrochemical measurements were performed in a Teflon electrochemical cell with CaF₂ optical

windows (3 mm thick). The potential of the n-SrTiO₃ photoelectrode with respect to an Ag/AgCl (3 M KCl) reference electrode (MF-2052; Basi, West Lafayette, IN) was controlled by a CHI650E Potentiostat (CH Instruments, Austin, TX). A Pt wire served as the counter electrode. Ohmic contact between the unpolished n-SrTiO₃ backside and copper wire (working electrode) was established using Gallium–Indium eutectic (Sigma-Aldrich, St. Louis, MO). For the transient reflectance experiments, an insulating lacquer covered all surfaces except the polished front side of the crystal. The exposed front surface areas of the 0.1% and Nb- doped samples accessible by the probe was $\approx 70 \text{ mm}^2$ on all samples that were used.

Transient Reflectance Measurements. For the transient experiments, the pump and probe beams were derived from a regeneratively amplified Ti:sapphire laser system (Coherent Legend; Coherent, Inc., Santa Clara, CA) producing pulses with a center wavelength of 800 nm and ≈ 150 fs temporal width at a 1 kHz repetition rate. Part of the amplifier output was directed into a third harmonic generation setup (Eksma FK-800–200-M, Vilnius, Lithuania) to generate 266 nm light as the pump. The pump beam was incident normal to the sample surface. In all experiments, the pump beam was modulated by a mechanical chopper (3501; Newport, Inc., Irvine, CA) at a frequency of 500 Hz. The incident pump fluence was measured to be 0.04 mJ cm^{-2} , corresponding to carrier densities on the order of 10^{13} cm^{-2} for all sets of transient reflection experiments.

Another part of the 800 nm beam was focused into a 5 mm thick CaF₂ crystal to generate a white light continuum (WLC) probe. The CaF₂ crystal was mounted on a stage which rotated the crystal to avoid burning and to generate a stable WLC. The portion of the WLC that we take into consideration ranges from 365 nm to 730 nm with different intensity for different wavelengths, with 500 nm being the most intense. The leftover fundamental (800 nm) was cut out using an 800 nm Notch Filter before the probe hits the sample. In order to reduce ghosting artifacts, the broadened portion of the fundamental was cut out with a solution of two dyes (NIR783C & NIR836C) obtained from QCR Solutions in a cuvette after the probe hits the sample. The incident angle of the probe on the sample is determined to be 35° using the reflection of the sample and the refractive index of water. The polarization of the WLC probe beam was controlled and made to be s polarized with respect to the table by changing the 800 nm polarization using a 1/2-wave plate and a linear polarizer. After the sample, the reflected probe beam was focused into an imaging spectrograph (Isoplan) and CCD Imaging Camera (PIXIS) setup from Princeton Instruments. In addition, $<10\%$ of the probe was split before the sample for referencing. Referencing was performed with an un-matched CMOS UltraFast Systems spectrometer using the smart referencing algorithm⁴⁸ with a 64 compressed pixel array⁴⁹ to achieve a differential probe stability of approximately 2 mOD per pulse pair. The detector outputs were interfaced with a personal computer, which provided automated control over an optical pump–probe delay stage (MTM250CC1; Newport, Inc., Irvine, CA). The probe beam spot size was measured to be 200 μm (fwhm) horizontally and 50 μm (fwhm) using knife edge measurements.

Laser Fluence of 0.04 mJ/cm^2 . All spectro-electrochemical measurements were performed with a fluence of 0.04 mJ/cm^2 . The fluence was calculated using the pulse energy and the area of the pump beam at the focus. The incident power, measured using a pyroelectric energy sensor (919E-200U-8-25K) from Newport. The pump beam size at the focus was measured by knife edge measurements to be 650 μm x 100 μm (fwhm) (Fig. S1). The beam was assumed to be spatially gaussian and the beam focal area was calculated by assuming an elliptical cross section.

Sample Stage Motion. A kinematic mirror mount was attached to the back of the electrochemical cell to allow for proper orientation of the sample surface with respect to the incidence plane of the probe. The

whole assembly was mounted on a 3-axis stage controlled by programmable actuators (Z 825 B; Thorlabs, Inc.) and controllers (TDC001; Thorlabs, Inc.) to move the illuminating spot on the sample continuously during all transient reflection experiments (see below), unless otherwise noted. The continuous scanning method was adopted for all transient reflectance experiments to obtain high quality data. The continuous movement of the sample allows us to minimize the sample degradation and maintain a stable current of 1.2 mA throughout the experiment (Fig. S2). The experiments are carried out by moving the stage such that the illuminating spot raster scans the sample at a controllable speed of 7 $\mu\text{m/s}$, unless stated otherwise. A scan speed of 7 $\mu\text{m/s}$ allows us to do 2 repeats of the experiment with 2.5 seconds of averaging per delay point (108 delays per repeat) on a single row of the sample (approximately 8 mm of working space/row). One full data set comprises of 2 experiments done at two different grating positions with 4 consecutive repeats in each experiment.

Electrolyte Solutions. The solutions used were within the range of pH 7 – pH 14 with sodium hydroxide (Sigma Aldrich). The unbuffered solutions were made simply by varying the sodium hydroxide concentration as needed. The buffered solutions were made primarily using sodium monobasic or dibasic phosphate (Sigma Aldrich) and sodium hydroxide. The pH of the solutions was measured by a calibrated pH meter (Catalog number 13620631 from Fisher Scientific). In all unbuffered solutions of pH less than or equal to pH 13, the sodium ion concentration was controlled and kept at 100 mM by adding sodium sulfate (Sigma Aldrich). Ionic strength is represented only by the sodium ion concentration of the solution in question. In all unbuffered solutions of pH less than or equal to pH 13, the sodium ion concentration was controlled and kept at 100 mM by adding sodium sulfate (Sigma Aldrich). The kinetic isotope effect experiments were carried out in unbuffered pD 7 and pD 13 conditions twice. The first time it was carried out with 200 mM sodium ion concentration using anhydrous sodium sulfate salt. 100 mM sodium ion concentration was maintained the second time. pD 7 solution was composed of 99% deuterated water (DLM 7005; Cambridge Isotope Labs) and anhydrous sodium sulfate. pD 13 solution was composed of sodium deuterioxide (DLM 57-50; Cambridge Isotope Labs) diluted with deuterated water and anhydrous sodium sulfate. The pD of the solutions was measured before and after the experiment and a correction of 0.456 was applied (for alkaline conditions) to the value obtained from the pH meter.

Acknowledgements: The experimental work were supported by the Director, Office of Science, Office of Basic Energy Sciences, and by the Division of Chemical Sciences, Geosciences and Biosciences of the U.S. Department of Energy at RASEI (Boulder, CO) under Contract No. DE-SC0018939. This included full support for one postdoctoral fellow and one graduate student, and partial support for another postdoctoral fellow and graduate student. We thank C.D. Pemmaraju and H. Frei for helpful discussions.

References:

1. Hammer, B.; Norskov, J. K., Theoretical surface science and catalysis--calculations and concepts. *Advances in Catalysis* **2004**, *45*, 71-129.
2. Markovic, N. M., Electrocatalysis: Interfacing electrochemistry. *Nature materials* **2013**, *12* (2), 101-2.
3. Seh, Z. W.; Kibsgaard, J.; Dickens, C. F.; Chorkendorff, I.; Norskov, J. K.; Jaramillo, T. F., Combining theory and experiment in electrocatalysis: Insights into materials design. *Science* **2017**, *355* (6321).
4. Weckhuysen, B. M., Chemical Imaging of Spatial Heterogeneities in Catalytic Solids at Different Length and Time Scales. *Angew. Chem.-Int. Edit.* **2009**, *48* (27), 4910-4943.

5. Buurmans, I. L. C.; Weckhuysen, B. M., Heterogeneities of individual catalyst particles in space and time as monitored by spectroscopy. *Nat. Chem.* **2012**, *4* (11), 873-886.
6. Rossmeisl, J.; Qu, Z. W.; Zhu, H.; Kroes, G. J.; Nørskov, J. K., Electrolysis of water on oxide surfaces. *Journal of Electroanalytical Chemistry* **2007**, *607* (1-2), 83-89.
7. Nørskov, J. K.; Bligaard, T.; Hvolbaek, B.; Abild-Pedersen, F.; Chorkendorff, I.; Christensen, C. H., The nature of the active site in heterogeneous metal catalysis. *Chem. Soc. Rev.* **2008**, *37* (10), 2163-2171.
8. Zhang, M.; Frei, H., Towards a Molecular Level Understanding of the Multi-Electron Catalysis of Water Oxidation on Metal Oxide Surfaces. *Catalysis Letters* **2014**, *145* (1), 420-435.
9. Kern, J.; Chatterjee, R.; Young, I. D.; Fuller, F. D.; Lassalle, L.; Ibrahim, M.; Gul, S.; Fransson, T.; Brewster, A. S.; Alonso-Mori, R.; Hussein, R.; Zhang, M.; Douthit, L.; de Lichtenberg, C.; Cheah, M. H.; Shevela, D.; Wersig, J.; Seuffert, I.; Sokaras, D.; Pastor, E.; Weninger, C.; Kroll, T.; Sierra, R. G.; Aller, P.; Butryn, A.; Orville, A. M.; Liang, M.; Batyuk, A.; Koglin, J. E.; Carbajo, S.; Boutet, S.; Moriarty, N. W.; Holton, J. M.; Dobbek, H.; Adams, P. D.; Bergmann, U.; Sauter, N. K.; Zouni, A.; Messinger, J.; Yano, J.; Yachandra, V. K., Structures of the intermediates of Kok's photosynthetic water oxidation clock. *Nature* **2018**, *563* (7731), 421-425.
10. Man, I. C.; Su, H.-Y.; Calle-Vallejo, F.; Hansen, H. A.; Martínez, J. I.; Inoglu, N. G.; Kitchin, J.; Jaramillo, T. F.; Nørskov, J. K.; Rossmeisl, J., Universality in Oxygen Evolution Electrocatalysis on Oxide Surfaces. *ChemCatChem* **2011**, *3* (7), 1159-1165.
11. Busch, M.; Halck, N. B.; Kramm, U. I.; Siahrostami, S.; Krttil, P.; Rossmeisl, J., Beyond the top of the volcano? – A unified approach to electrocatalytic oxygen reduction and oxygen evolution. *Nano Energy* **2016**, *29*, 126-135.
12. Chen, X.; Choing, S. N.; Aschaffenburg, D. J.; Pemmaraju, C. D.; Prendergast, D.; Cuk, T., The formation time of Ti-O• and Ti-O•-Ti radicals at the n-SrTiO₃/aqueous interface during photocatalytic water oxidation. *Journal of the American Chemical Society* **2017**, *139*, 1830-1841.
13. Herlihy, D. M.; Waegle, M. M.; Chen, X.; Pemmaraju, C. D.; Prendergast, D.; Cuk, T., Detecting the oxyl radical of photocatalytic water oxidation at an n-SrTiO₃/aqueous interface through its subsurface vibration. *Nat Chem* **2016**, *8* (6), 549-55.
14. Zhang, M.; de Respinis, M.; Frei, H., Time-resolved observations of water oxidation intermediates on a cobalt oxide nanoparticle catalyst. *Nat Chem* **2014**, *6* (4), 362-7.
15. Zandi, O.; Hamann, T. W., Determination of photoelectrochemical water oxidation intermediates on hematite electrode surfaces using operando infrared spectroscopy. *Nat. Chem.* **2016**, *8* (8), 778-83.
16. Cheng, J.; VandeVondele, J.; Sprik, M., Identifying Trapped Electronic Holes at the Aqueous TiO₂ Interface. *J. Phys. Chem. C* **2014**, *118* (10), 5437-5444.
17. Chen, J.; Li, Y. F.; Sit, P.; Selloni, A., Chemical Dynamics of the First Proton-Coupled Electron Transfer of Water Oxidation on TiO₂ Anatase. *Journal of the American Chemical Society* **2013**, *135* (50), 18774-18777.
18. Kraack, J. P.; Hamm, P., Surface-Sensitive and Surface-Specific Ultrafast Two-Dimensional Vibrational Spectroscopy. *Chemical Reviews* **2017**, *117* (16), 10623-10664.
19. Kraack, J. P.; Kaech, A.; Hamm, P., Surface Enhancement in Ultrafast 2D ATR IR Spectroscopy at the Metal-Liquid Interface. *The Journal of Physical Chemistry C* **2016**, *120* (6), 3350-3359.
20. Klahr, B.; Gimenez, S.; Fabregat-Santiago, F.; Bisquert, J.; Hamann, T. W., Photoelectrochemical and Impedance Spectroscopic Investigation of Water Oxidation with "Co-Pi"-Coated Hematite Electrodes. *J. Am. Chem. Soc.* **2012**, *134* (40), 16693-16700.
21. Chen, X.; Aschaffenburg, D. J.; Cuk, T., Selecting between two transition states by which water oxidation intermediates decay on an oxide surface. *Nature Catalysis* **2019**, *2* (9), 820-827.
22. Libuda, J.; Meusel, I.; Hartmann, J.; Freund, H. J., A molecular beam/surface spectroscopy apparatus for the study of reactions on complex model catalysts. *Rev. Sci. Instrum.* **2000**, *71* (12), 4395-4408.

23. Parsons, R., The rate of electrolytic hydrogen evolution and the heat of adsorption of hydrogen. *Transactions of the Faraday Society* **1958**, 54 (0), 1053-1063.
24. Aschaffenburg, D. J.; Chen, X.; Cuk, T., Faradaic oxygen evolution from SrTiO₃ under nano- and femto-second pulsed light excitation. *Chem Commun (Camb)* **2017**, 53 (53), 7254-7257.
25. Xu, Y.; Schoonen, M. A. A., The absolute energy positions of conduction and valence bands of selected semiconducting minerals. *American Mineralogist* **2000**, 85 (3-4), 543-556.
26. Janotti, A.; Varley, J. B.; Choi, M.; Van de Walle, C. G., Vacancies and small polarons in SrTiO₃. *Phys. Rev. B* **2014**, 90 (8), 085202.
27. Chen, H.; Umezawa, N., Hole localization, migration, and the formation of peroxide anion in perovskite SrTiO₃. *Physical Review B* **2014**, 90 (3).
28. Rubano, A.; Paparo, D.; Granozio, F. M.; Uccio, U.; Marrucci, L., Blue luminescence of SrTiO₃ under intense optical excitation. *Journal of Applied Physics* **2009**, 106, 103515.
29. Mochizuki, S.; Fujishiro, F.; Minami, S., Photoluminescence and reversible photo-induced spectral change of SrTiO₃. *Journal of Physics: Condensed Matter* **2005**, 17 (6), 923-948.
30. Schirmer, O. F., O-bound small polarons in oxide materials. *Journal of Physics: Condensed Matter* **2006**, 18 (43), R667-R704.
31. Deskins, N. A.; Dupuis, M., Intrinsic Hole Migration Rates in TiO₂ from Density Functional Theory. *The Journal of Physical Chemistry C* **2009**, 113 (1), 346-358.
32. Formal, F. L.; Pastor, E.; Tilley, D.; Mesa, C. A.; Pendlebury, S. R.; Gratzel, M.; Durrant, J. R., Rate Law Analysis of Water Oxidation on a Hematite Surface. *J. Am. Chem. Soc.* **2015**, 137, 6629-6637.
33. Kafizas, A.; Ma, Y.; Pastor, E.; Pendlebury, S. R.; Mesa, C.; Francàs, L.; Le Formal, F.; Noor, N.; Ling, M.; Sotelo-Vazquez, C.; Carmalt, C. J.; Parkin, I. P.; Durrant, J. R., Water Oxidation Kinetics of Accumulated Holes on the Surface of a TiO₂ Photoanode: A Rate Law Analysis. *ACS Catalysis* **2017**, 7 (7), 4896-4903.
34. Waagele, M. M.; Chen, X.; Herlihy, D. M.; Cuk, T., How Surface Potential Determines the Kinetics of the First Hole Transfer of Photocatalytic Water Oxidation. *J. Am. Chem. Soc.* **2014**, 136 (30), 10632-10639.
35. Mandal, A.; Ramasesha, K.; Marco, L. D.; Tokmakoff, A., Collective vibrations of water-solvated hydroxide ions investigated with broadband 2DIR spectroscopy. *The Journal of Chemical Physics* **2014**, 140 (20), 204508.
36. Baiz, C. R.; Peng, C. S.; Reppert, M. E.; Jones, K. C.; Tokmakoff, A., Coherent two-dimensional infrared spectroscopy: Quantitative analysis of protein secondary structure in solution. *Analyst* **2012**, 137 (8), 1793-1799.
37. Stewart, G. W., On the Early History of the Singular Value Decomposition. *SIAM Review* **1993**, 35 (4), 551-566.
38. Guhl, H.; Miller, W.; Reuter, K., Water adsorption and dissociation on SrTiO₃(001) revisited: A density functional theory study. *Physical Review B* **2010**, 81 (15).
39. Hinojosa, B. B.; Van Cleve, T.; Asthagiri, A., A first-principles study of H₂O adsorption and dissociation on the SrTiO₃(100) surface. *Mol. Simul.* **2010**, 36 (7-8), 604-617.
40. Holmstrom, A.; Spijker, P., and Foster, A.S., The interface of SrTiO₂ and H₂O from density functional theory molecular dynamics. *Proc. R. Soc. A.* **2016**, 472, 20160293.
41. Roberts, S. T.; Ramasesha, K.; Petersen, P. B.; Mandal, A.; Tokmakoff, A., Proton Transfer in Concentrated Aqueous Hydroxide Visualized Using Ultrafast Infrared Spectroscopy. *The Journal of Physical Chemistry A* **2011**, 115 (16), 3957-3972.
42. Marx, D.; Chandra, A.; Tuckerman, M. E., Aqueous Basic Solutions: Hydroxide Solvation, Structural Diffusion, and Comparison to the Hydrated Proton. *Chemical Reviews* **2010**, 110 (4), 2174-2216.
43. Perakis, F.; Widmer, S.; Hamm, P., Two-dimensional infrared spectroscopy of isotope-diluted ice Ih. *The Journal of Chemical Physics* **2011**, 134 (20), 204505.

44. De Marco, L.; Carpenter, W.; Liu, H.; Biswas, R.; Bowman, J. M.; Tokmakoff, A., Differences in the Vibrational Dynamics of H₂O and D₂O: Observation of Symmetric and Antisymmetric Stretching Vibrations in Heavy Water. *The Journal of Physical Chemistry Letters* **2016**, 7 (10), 1769-1774.
45. Swenson, H.; Stadie, N. P., Langmuir's Theory of Adsorption: A Centennial Review. *Langmuir* **2019**, 35 (16), 5409-5426.
46. Cheng, J.; Vandevondele, J.; Sprik, M., Identifying trapped electronic holes at the aqueous TiO₂ interface. *J. Phys. Chem. C* **2014**, 118, 5437-5444.
47. Cheng, J.; Sprik, M., Acidity of the Aqueous Rutile TiO₂(110) Surface from Density Functional Theory Based Molecular Dynamics. *Journal of Chemical Theory and Computation* **2010**, 6 (3), 880-889.
48. Feng, Y.; Vinogradov, I.; Ge, N.-H., General noise suppression scheme with reference detection in heterodyne nonlinear spectroscopy. *Opt. Express* **2017**, 25 (21), 26262-26279.
49. Feng, Y.; Vinogradov, I.; Ge, N.-H., Optimized noise reduction scheme for heterodyne spectroscopy using array detectors. *Opt. Express* **2019**, 27 (15), 20323-20346.